Journal of Materials Chemistry C

A novel reversible fluorescent probe for the highly sensitive detection of nitro and peroxide organic explosives using electrospun $BaWO_4$ nanofibers

Journal:	*Journal of Materials Chemistry C*
Manuscript ID	TC-ART-09-2019-005068.R2
Article Type:	Paper
Date Submitted by the Author:	29-Oct-2019
Complete List of Authors:	George, Gibin; Fayetteville State University, Chemistry, Physics and Material Science Edwards, Caressia; Fayetteville State University, Chemistry, Physics and Material Science Hayes, Jacob; Fayetteville State University, Chemistry, Physics and Material Science Yu, Lei; Argonne National Laboratory; Nanjing University of Science and Technology Ede, Sivasankara Rao ; Fayetteville State University, Chemistry, Physics and Material Science Wen, Jianguo; Argonne National Laboratory, Electron Microscopy Center Luo, Zhiping; Fayetteville State University, Chemistry, Physics and Material Science

ARTICLE

A novel reversible fluorescent probe for the highly sensitive detection of nitro and peroxide organic explosives using electrospun $BaWO_4$ nanofibers

Received 00th January 20xx,
Accepted 00th January 20xx

DOI: 10.1039/x0xx00000x

Gibin George,[a] Caressia S. Edwards,[a] Jacob I. Hayes,[a] Lei Yu,[b] Sivasankara Rao Ede,[a] Jianguo Wen,[b] Zhiping Luo*[a]

Fabrication of highly stable, reversible, and efficient portable sensors for the detection of explosives for safety and security is challenging due to the robustness of the currently available detection tools, limiting their mass deployment to the explosive prone areas. This paper reports a new direction towards the sensing of nitro- and peroxide-based explosives using highly stable rare-earth-doped $BaWO_4$ nanofibers with remarkable sensitivity and reversibility. $BaWO_4$ nanofibers doped with Tb^{3+} and Eu^{3+} ions are fabricated through a sol-gel electrospinning process, and their emission characteristics and application as a fluorescent probe for the sensing of 2-nitrotoluene and H_2O_2, explosive taggants representing a broad class of explosives, are studied in detail. Scheelite structured $BaWO_4$ nanofibers exhibit excellent luminescent characteristics, and the rare-earth ion doping in the polycrystalline $BaWO_4$ nanofibers is tailored to achieve blue, green, red, and white light emissions. These nanofibers are extremely sensitive to 2-nitrotoluene and H_2O_2 with rapid response time, and sensitivity is observed within the range of 1−400 ppb and 1−10 ppm, towards 2-nitrotoluene and H_2O_2, respectively. The fluorescent quenching of $BaWO_4$ nanofibers in the presence of 2-nitrotoluene and H_2O_2 is exponential with the quenching constants up to 1.73×10^6 and 2.73×10^4 $L\cdot mol^{-1}$, respectively, which is significantly higher than most of the fluorescent probes based on metal-organic frameworks and conjugated organic materials. The luminescence of the nanofibers is retained completely after exposing to 2-nitrotoluene upon heating at 120 °C for 10 min and the sensory response is retained as fresh nanofibers, and currently available fluorescent explosive sensors could not achieve such a recovery. The high sensitivity and selectivity of scalable rare-earth-doped $BaWO_4$ nanofibers provide a new platform for the simultaneous detection of two classes of explosives.

Introduction

In recent years, for the sake of safety and security, the interest in the detection and quantification of nitro-organic compounds and organic peroxides, primary classes of explosives, is increased tremendously across the world. The current analytical techniques such as liquid chromatography-mass spectrometry (LC-MS), gas chromatography-mass spectrometry (GC-MS), high-performance liquid chromatography (HPLC), ion mobility spectrometry, proton transfer reaction mass spectrometry (PTR-MS), electrochemical methods, surface plasmon resonance (SPR), and surface-enhanced Raman scattering (SERS),[1] etc. for the detection of explosives requires specialized training and miniaturization of such techniques is nearly infeasible. Therefore, fluorescence-based explosive sensors have been extensively studied for miniaturized portable devices,[2] especially, florescent nanostructured materials such as quantum dots[3] and metal-organic frameworks.[4] Developing a sensitive and selective sensor for the explosives, which is inexpensive and portable, is always of practical significance.

An explosive sensor requires exceptionally high sensitivity and low limit of detection (LOD) because of the very low vapor pressures of these compounds. Additionally, high selectivity is necessary to avoid false signals and should be available for mass deployment to cover the breadth of terrorist threats involving explosives.[5] The major classes of explosives are organic nitro-compounds and organic peroxides. Due to the very low vapor pressures of these molecules, they are more likely to attach on surfaces with high surface energy such as metals, metal oxides, etc. as compared with low surface energy materials such as polymers, plastics, etc.[5] Moreover, the higher surface-to-volume ratio of the nanomaterials enhances the interaction between the analyte and the sensor material.[6]

Photoluminescence-based sensors have been widely reported for the detection and quantification of explosives traces.[7] The performances of these sensors are based on the characteristics of the sensory materials used, for instance, the ability of the sensor material to form a complex with the explosive molecules for photo-induced electron transfer (PET).[8] Besides, the overlapping of the emission spectrum of the

[a] Department of Chemistry, Physics and Material Science, Fayetteville State University, Fayetteville, NC 28301, USA. E-mail: zluo@uncfsu.edu
[b] Centre for Nanoscale Materials, Argonne National Laboratory, Argonne, IL 60439, USA

[c] Electronic Supplementary Information (ESI) available: [TGA results of precursor fibers, Rietveld refined XRD patterns, FTIR spectra and CIE diagram of $BaWO_4$ nanofibers]. See DOI: 10.1039/x0xx00000x

sensory material with the absorption spectrum of explosives is important in resonance energy transfer (RET)[9] and protonation of fluorophores by analytes is necessary for Intramolecular charge transfer (ICT).[10] The current organic fluorescent materials may be sensitive and efficient in determining nitro explosives; while their instability for repeated use is a significant concern.[11] The recovery of the luminescence of the hybrid organic sensor materials can be achieved only through the subsequent washing, and most of the time, the sensitivity cannot be completely recovered, as observed in the case of luminescent metal-organic frameworks (MOFs).[12] The shortcomings such as stability, color tunability, broad emission, etc. of luminescent sensors can be overcome using rare-earth (RE^{3+}) doped inorganic oxides and fluorides with sharp and tunable luminescent emission. The application of inorganic materials with high thermal and chemical stability and sharp emission is highly promising as fluorescent probes towards various chemicals. The recovery of the luminescence by these sensors is often possible by simply heating above the evaporation temperature of the explosive materials.

Scheelite structured materials are widely reported for their photophysical and photocatalytic activities.[13] Their photoluminescent sensing behavior is reported towards the sensitivity of H_2O_2 [6] and Glucose.[14] Scheelites with the general formula AWO_4 (A = Ba, Sr, Ca, Pb) are broadly studied for their luminescence, photocatalysis, and scintillation properties.[15] Among them, $BaWO_4$ is an important material, which is highly suitable for optical applications. For instance, $BaWO_4$ crystal is identified as an efficient Raman−active material for utilization in picosecond solid-state laser systems, due to their high Stokes conversion efficiency in stimulated Raman scattering.[16] Eu^{3+}-doped $BaWO_4$ nanowires can improve the efficiency of dye-sensitized solar cells, resulting in an increase in efficiency by 15% as compared to the cell without $BaWO_4$:Eu^{3+} nanowires.[17] $BaWO_4$ is reported for a large number of other optical applications, such as fluorescent sensors,[17] phosphors, light-emitting diodes, optical filters, scintillators, photocatalysis, and solid-state lasers.[18] The fabrication of $BaWO_4$ nanostructures with different morphologies and sizes has been reported in the literature, such as whiskers, nanowires, penniform nanostructures, nanosheets and nanobelts, hollow spheres, dumbbell, and ellipsoids.[19] Nevertheless, electrospun $BaWO_4$ nanostructures with very high aspect ratios, and their properties are nowhere reported in the literature.

One-dimensional nanoscale architectures are successfully integrated into nanoscale devices based on the optical, magnetic, and electronic properties of the materials.[17] Electrospinning is a widely accepted technique for the scalable fabrication of organic and inorganic nanofibers for many applications. The high aspect ratio nanofibers have enhanced performances in terms of charge and energy transport compared to bulk materials or two-dimensional systems.[20] Thus, luminescent organic/inorganic nanofibers are enticing a growing demand for the development of nanoscale light-emitting devices with high efficiency. Electrospun nanofibers are potential candidates for highly sensitive optical biosensors,[21] nanoscale optical waveguides,[22] optical filters,[23] excitation source for lab on chip microfluidic devices,[24] and novel laser architectures.[25] Besides, electrospinning has a high throughput, versatile, cost-effective, and easy control of the shape and size of one-dimensional nanoscale architectures as compared to many conventional techniques.

In this work, we report the fabrication of ultra-long $BaWO_4$ nanofibers through a sol-gel electrospinning process and their sensitivity toward the detection of explosive taggants. The PL emission bands of the $BaWO_4$ nanofibers are tailored by Tb^{3+}, and Eu^{3+} doping and the RE^{3+} loading is optimized for white light emission. The cathodoluminescent (CL) emission of these nanofibers under high-energy electron beam irradiation is also studied for the potential application in high-energy radiation detection. RE^{3+} doped nanofibers are highly sensitive to 2-nitrotoluene with the LOD of 35−45 nM, which is lower than MOF based sensors[12b,26] and comparable to that of CdSe quantum dots.[27] The fluorescent quenching of the nanofibers in the presence of analytes is reversible, and the nanofibers are successfully reused for the detection of the explosives after subsequent heating, and such a recovery is not observed in the case of fluorescent probes for explosives reported in the literature. $BaWO_4$ luminescent nanofibers offer a highly stable and promising miniaturized alternative to conventional analytical techniques and organic materials for precise and sensitive detection of explosives.

Materials and Methods

Materials

Polyvinylpyrrolidone (PVP) [MW: 1.0×10^6], barium (II) acetate ($Ba(Ac)_2$), ammonium metatungstannate (AMT, assay 98%), and N, N−dimethylformamide (DMF) purchased from Sigma Aldrich were used without further purification to fabricate the precursor composite fibers. Europium acetate hydrate procured from Sigma Aldrich, and terbium acetate hydrate from Alfa Aesar were used for RE^{3+} doping. H_2O_2 (50 W%) obtained from Acros organics and 2-nitrotoluene from Merck were used as the model explosives for sensing.

Electrospinning of $BaWO_4$ nanofibers

To prepare electrospinnable sol of PVP and the metal salts, the predetermined amounts of the acetate salts were dissolved in 20/80 water/DMF mixed solvent. To the above solution, ten w/v% of PVP was added and stirred magnetically for 10 min. Finally, the stoichiometric quantity of AMT was added and stirred overnight before it was loaded to the electrospinning unit (MSK−NFES−4, MTI Corporation). The electrospinning was carried out under an applied voltage of 18 kV, a tip to collector distance of 17 cm, and a solution flow rate of 500 µL h^{-1}. The precursor composite fibers were collected on a rotating drum collector plate covered with an aluminum foil. The selection of the calcination temperature was based on the degradation temperature of the precursor composite fibers during their thermogravimetric analysis (TGA) (Shimadzu DTG−60) in a nitrogen atmosphere at a heating rate of 10 °C min^{-1}. The electrospun PVP/$Ba(Ac)_2$/AMT composite nanofibers were then

calcined at 700 °C, at a heating rate of 2 °C min^{-1} with a dwell time of 5 h to obtain $BaWO_4$ nanofibers. The doped nanofibers were made using a similar method, in which respective molar percentage of acetate salts of the dopants are added to replace the subsequent amount of $Ba(Ac)_2$, and the procedure above was followed. All the doped $BaWO_4$ nanofibers were calcined at 700 °C. The doped nanofibers are represented as $BaWO_4$:*x*Tb−*y*Eu, where *x* and *y* are the respective mol.% of RE^{3+} ions.

Characterization of $BaWO_4$ nanofibers

The morphology of the $BaWO_4$ nanowires was identified using JEOL field-emission JXA−8530F electron probe microanalyzer (EPMA), after coating the samples with ~5 nm carbon film (Denton carbon coater). EPMA was equipped with an X-ray energy dispersive spectrometer (EDS) for chemical compositional analysis, and an xCLent IV Advanced B Hyperspectral Cathodoluminescence (CL) detector for the CL analysis. The nanofibers for transmission electron microscopy (TEM) were prepared in pure ethanol solutions, sonicated for 1 min and then dispersed on carbon−film supported grids. The grids were observed in FEI Talos F200X TEM/STEM instrument at 200 kV. The scanning TEM (STEM) imaging was done in the STEM mode using a high-angle annular dark-field imaging (HAADF) detector, and the elemental maps of selected elements were collected using the X-ray EDS signals. The X-ray diffraction (XRD) patterns of the nanofibers were recorded using Rigaku MiniFlex 600 X-ray diffractometer in a scan range of 10−90° and a scan speed 0.06 deg min^{-1}. Fourier−transform infrared (FTIR) spectra (IRPrestige−21, Shimadzu) were recorded in transmission mode by the KBr pellet method in the wavenumber range of 300–4,000 cm^{-1} at an average of 32 scans. The photoluminescent spectra of the samples were obtained in powder form recorded using Shimadzu RF−5301PC spectrofluorophotometer at room temperature, and the sensitivity measurements were also performed using the same instrument.

Sensitivity measurements

To test the sensitivity towards the explosives, 2-nitrotoluene and H_2O_2 were used as the detection taggants. 5 mg of the $BaWO_4$ nanofiber phosphor was dispersed in 50 mL of deionized water, and the concentration of 2−nitrotoluene and H_2O_2 were subsequently adjusted in the solution, and the PL emission spectra were recorded for different concentration of taggants. To test the selectivity, the PL emissions from the nanowires in the presence of $Cu(NO_3)_2$ (Cu^{2+}), $Fe(NO_3)_3$ (Fe^{3+}), glucose, $AgNO_3$ (Ag^+), $Ba(NO_3)_2$ (Ba^{2+}), $Pb(NO_3)_3$ (Pb^{2+}), $Cr(NO_3)_3$ (Cr^{3+}), HCl (2 pH) and NaOH (14 pH) were recorded. The selectivity towards other nitro-aromatic compounds is studied using 4-nitrotoluene and 3-nitrophenol as the representative analytes. To study the sensitivity of the nanofibers in the solid-state, the nanofibers are pasted on a glass substrate using SCOTCH double-sided tape. The nanofibers are then exposed to 2-nitrotoluene vapors generated by heating the appropriate quantities of *2*- nitrotoluene in a petri dish. The PL spectra of the nanofibers are then recorded. The 2-nitrotoluene vapors from the nanofibers were removed by heating at 120 °C for 10 minutes in a conventional oven and the PL spectra is recorded. The process is repeated up to 10 times to check the reversibility of the fibers in detecting the nitroaromatic compounds.

Results and Discussions

The TGA and DTA plots of PVP/$Ba(Ac)_2$/AMT composite nanofibers are shown in Fig. S1. The precursor composite nanofibers exhibit three−steps in their thermal degradation process before it is completely transformed into $BaWO_4$ nanofibers, whereas the pure PVP exhibit a single step in its thermal degradation profile.[28] The actual onset of degradation of the composite nanofibers is at ~250 °C and the degradation

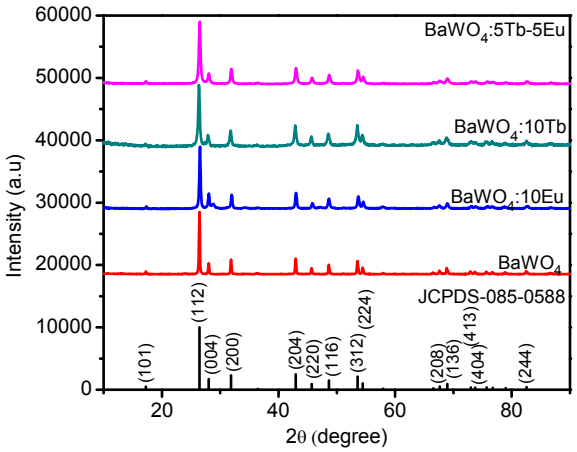

Fig. 1. Comparison of XRD patterns of pure and doped $BaWO_4$ nanofibers calcined at 700 °C.

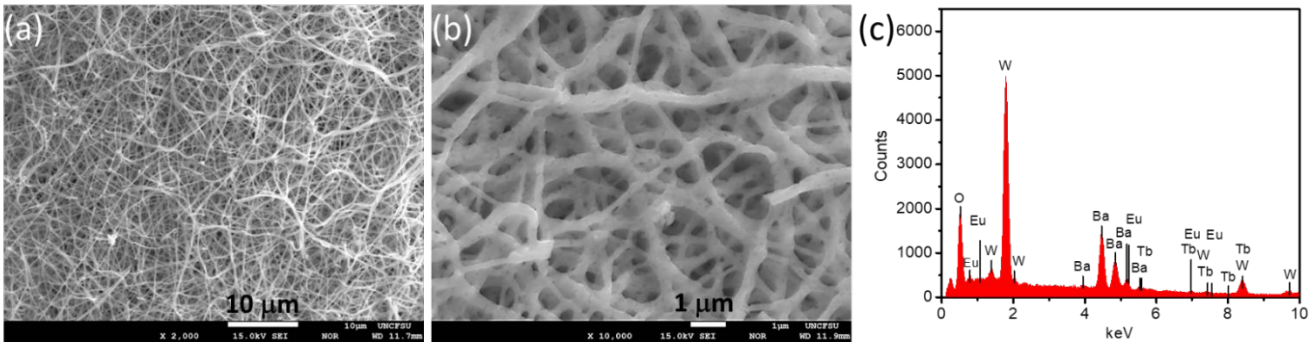

Fig. 2. (a) Low and (b) high magnification SEM images of representative $BaWO_4$ nanofibers; (c) EDS spectrum of $BaWO_4$:5Tb−5Eu nanofibers.

is completed at ~475 °C. The removal of water from the nanofibers is evident in the first step of the degradation process at ~100 °C. The conversion of the organic part of the salts commences during the second step of the degradation process at ~250 °C. The complete elimination of the volatile part of the salts and PVP takes place in the final step. The DTA curve exhibit multiple exothermic and endothermic phase transformations during the degradation process. Though there is no remarkable weight loss above 475 °C, the exothermic reaction continues at high temperatures as evident from the DTA peaks above 500 °C, which essentially tells the calcination temperature as ~700 °C.

Morphology and Structure

The successful formation of pure and RE^{3+} doped $BaWO_4$ nanofibers from the precursor composite nanofibers was confirmed with the XRD results shown in Fig. 1. The $BaWO_4$ nanofibers obtained after calcination is completely crystalline as indicated by the very sharp peaks in the XRD patterns of the nanofibers. The structure of $BaWO_4$ nanofibers can be indexed to JCPDS standard data file No. 01−085−0588, with a space group of $I4_1/a$ (No. 88) (a = 5.613 Å and c = 12.72 Å). XRD patterns of the RE^{3+} doped $BaWO_4$ nanofibers reveals that the crystal structure of $BaWO_4$ remains unaffected by the dopants since there is no apparent peak of the dopant oxide in the XRD pattern of the respective nanofibers. Table 1 lists the lattice parameters and cell volume of $BaWO_4$:RE^{3+} nanofibers obtained by Rietveld refinement of the XRD patterns, as shown in Fig. S2.

The RE^{3+} ions are replacing the lattice site of Ba^{2+} ions, and the size of RE^{3+} ions are smaller than the Ba^{2+} ions. Therefore, a change in the lattice parameter and the reduction in unit cell

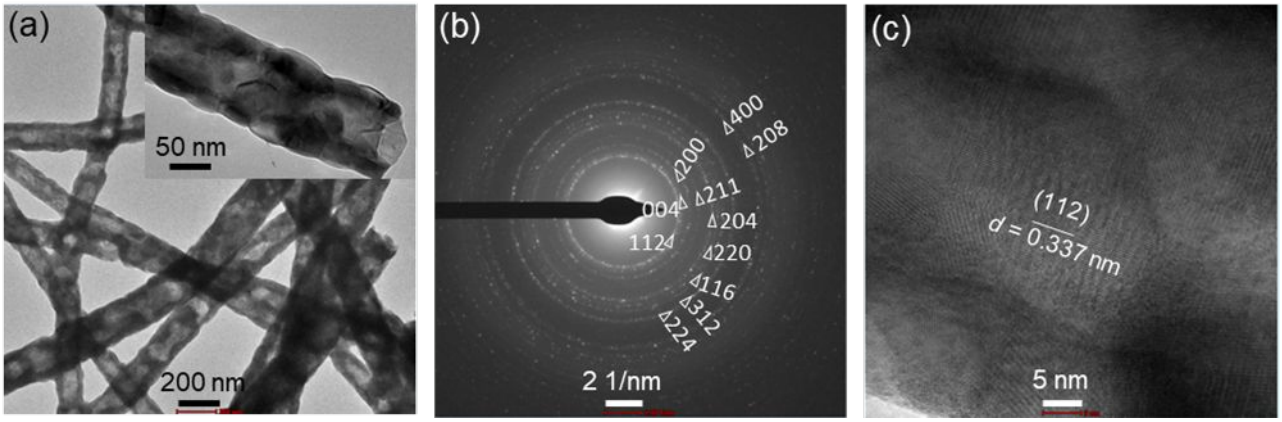

Fig. 3. (a) TEM, (b) SAED pattern, and (c) HRTEM images of $BaWO_4$:5Tb−5Eu nanofibers.

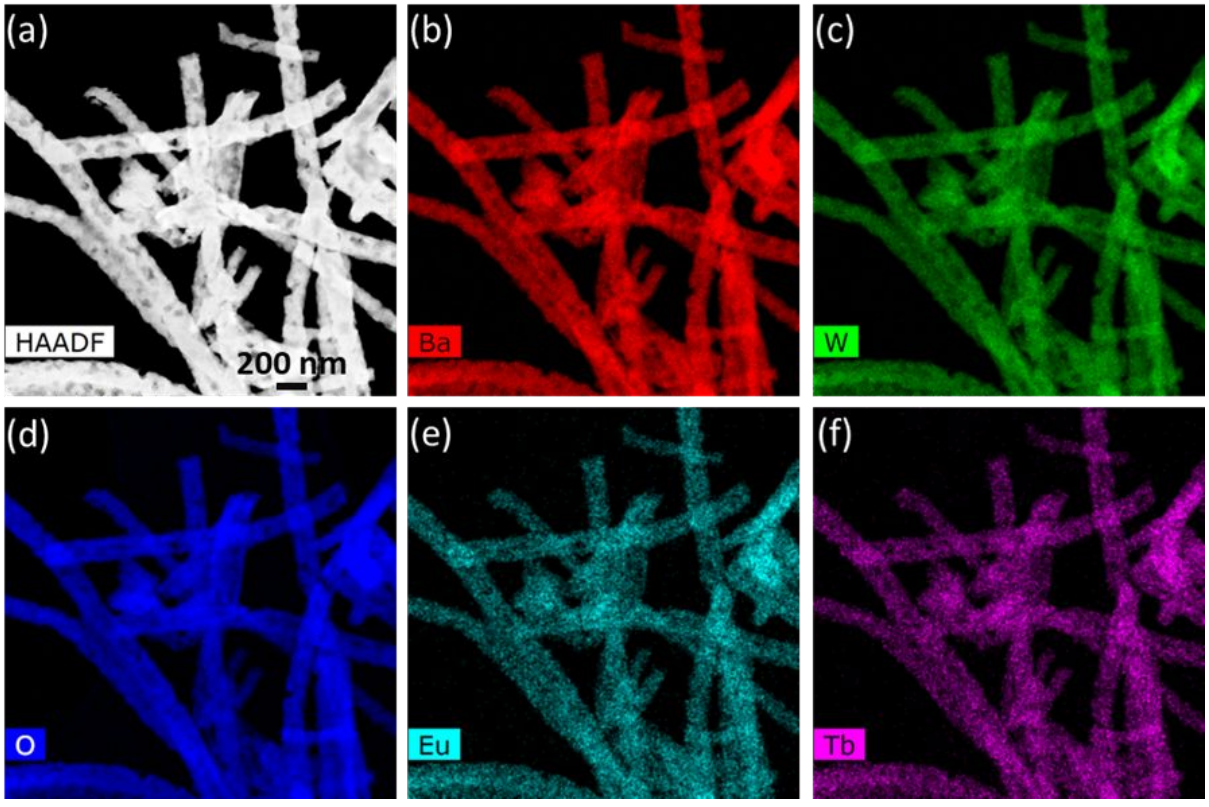

Fig. 4. (a) TEM-HAADF image and (b)-(f) are the corresponding elemental maps by EDS of $BaWO_4$:5Tb-5Eu nanofibers.

volume is expected, and the same is observed during the refinement. Fig. 2a&b shows the electrospun $BaWO_4$ nanofibers obtained after calcining at 700 °C. The SEM images reveal that the fibers are randomly oriented and continuous. The high magnification images reveal the porous nature of the fibers. In the EDS spectrum of the representative (Fig. 2c) nanofibers, the peaks corresponding to Ba, W and O, and the representative dopants are present.

Table 1 Lattice parameters and volume cell of $BaWO_4$:Re^{3+} nanofibers.

Sample	Lattice parameter (Å)		Volume
	a	*c*	(Cubic Å)
BaWO4	5.6232	12.7437	402.96
BaWO4:Tb	5.6108	12.7603	401.71
BaWO4:5Eu	5.6114	12.7331	400.94
BaWO4:5Tb–5Eu	5.6095	12.7257	400.43

The representative TEM images of the $BaWO_4$ nanofibers are shown in Fig. 3. The TEM images reveal that the nanofibers are of 156 nm in average diameter with a standard deviation of 10.6 nm, based on 20 measurements, and polycrystalline in nature, with a grain size of ~30 nm (Fig. 3a inset). The rings in the SAED pattern in Fig. 3b also reveals the polycrystalline nature of the nanofibers with high crystallinity. The nanosized grains composing the fibers are randomly oriented, and they are formed due to homogeneous nucleation and the space confinement of the nanofibers.[29] The measured *d*–spacings from the high-resolution TEM (HRTEM) image (Fig. 3c) are consistent with the XRD results. The TEM-EDS elemental maps of the $BaWO_4$:5Tb-5Eu nanofibers shown in Fig. 4 reveal that the Tb^{3+} and Eu^{3+} ions are uniformly dispersed in the $BaWO_4$ nanofiber lattice.

The complete elimination of organic parts from the precursor composite fibers is confirmed with the FTIR spectra (Fig. S3). In the spectra of PVP/$Ba(Ac)_2$/AMT composite nanofibers, the broad peak at 3453 cm^{-1} is due to the –OH stretching. The peaks at 2,957 and 2,882 cm^{-1} represent the symmetric and asymmetric vibrations of CH in CH_2 and CH_3, respectively. The peaks 1,648, 1,411, and 1,288 cm^{-1} are attributed to C=O, CH_2 bending, and C≡N vibrations, respectively.[30] The broad peak between 800–400 cm^{-1} is due to the several vibrational modes of pyrrolidone ring.[31] The pure and doped nanofibers of $BaWO_4$ exhibit a significant broad peak at ~835 cm^{-1}. In $BaWO_4$, the $[WO_4]^{2-}$ ligand has T_d point group symmetry. Therefore, the irreducible vibrational modes can be written as $\Gamma_{Td} = A_1(\nu_1) + E(\nu_2) + F_2(\nu_3) + F_2(\nu_4)$, in which $F_2(\nu_3,\nu_4)$ modes are IR active. Hence, the peak at ~835 cm^{-1} can be assigned to $F_2(\nu_3)$ anti–symmetric stretching vibrations for $BaWO_4$.[32]

Photoluminescence

The PL and photoluminescence excitation (PLE) spectra of pure $BaWO_4$ and doped $BaWO_4$ nanofibers are shown in Fig. 5. On comparing the PLE spectra of pure and RE^{3+} doped nanofibers, one can observe the significant transition of the blue emission characteristic of $[WO_4]^{2-}$ ligands to green and red corresponding to Tb^{3+} and Eu^{3+}, respectively. The PLE spectra of pure $BaWO_4$ nanofibers exhibit a broad absorption peaking at 247 nm, for the emission monitored at 440 nm, which is characteristic of the $^1A_1$ ground state absorption of $[WO_4]^{2-}$ unit. The broad asymmetric blue-green PL spectra of $BaWO_4$ nanofibers

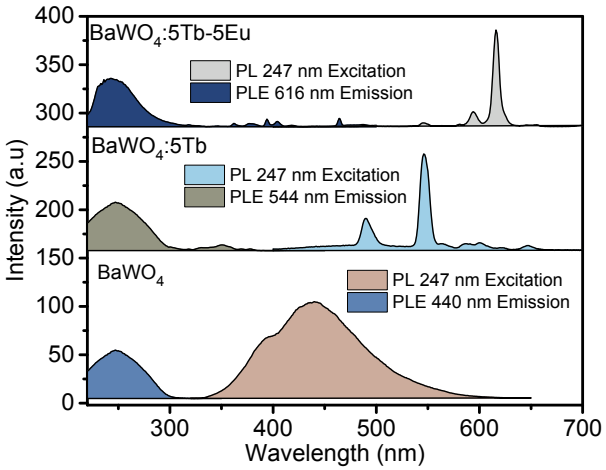

Fig. 5. PL and PLE spectra of pure $BaWO_4$ and RE^{3+} doped $BaWO_4$ nanofibers in the solid state.

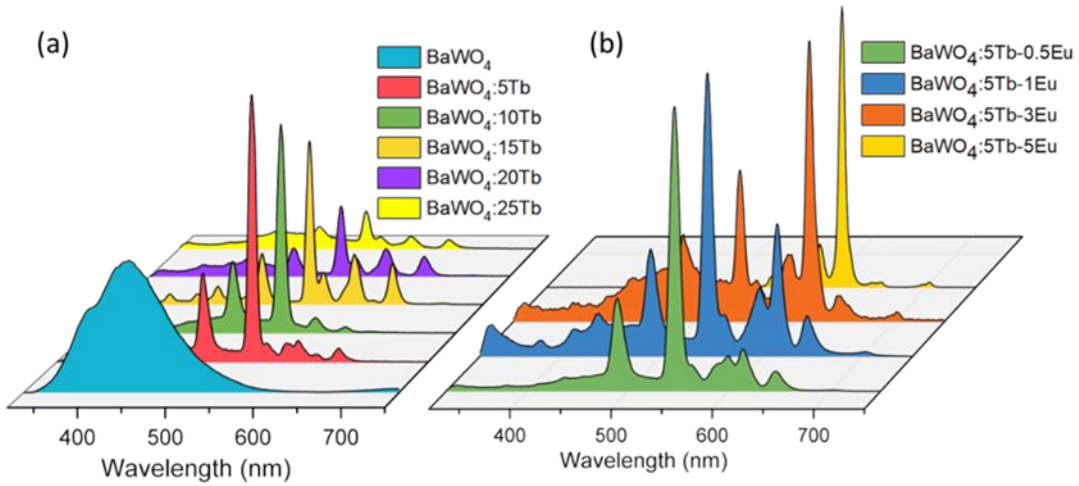

Fig. 6. PL spectra of (a) $BaWO_4$: *x*Tb and (b) $BaWO_4$:5Tb–*y*Eu nanofibers under 247 nm excitation in the solid state.

constitutes two peaks in the UV–blue region and blue-green region when excited by a 247 nm source. Which is originated by the charge transferring in the $[WO_4]^{2-}$ complexes with the T_d symmetry groups or self-trapped electron states.[33] In The case of $BaWO_4$:5Tb nanofibers, the PLE spectrum is monitored at 545 nm emissions, exhibit several bands between 250–400 nm originated by $4f^8 \rightarrow 4f^7 5d^1$ transition of Tb^{3+} ions.[34] However, the broad absorption peak of the host matrix is also present in the PLE spectra. The sharp peaks observed at 488, 544, 590 and 620 nm are originated from $^5D_4 \rightarrow {}^7F_6$, $^5D_4 \rightarrow {}^7F_5$, $^5D_4 \rightarrow {}^7F_4$, and $^5D_4 \rightarrow {}^7F_3$ $4f$–$4f$ transitions of Tb^{3+} ions, respectively.[35] On comparing the PLE spectra of $BaWO_4$:5Tb nanofibers with that of $BaWO_4$:5Tb–5Eu nanofibers, several additional peaks appeared in the latter, due to the intra–configurational f–f transitions of Eu^{3+}. In the respective PLE spectrum, in addition to the broad excitation peak of $BaWO_4$ matrix at 247 nm, dominant peaks at 364, 377, 394, 410 and 464 nm are also observed, which correspond to $^7F_0 \rightarrow {}^5D_4$, $^7F_0 \rightarrow {}^5G_2$, $^7F_0 \rightarrow {}^5L_6$, $^7F_0 \rightarrow {}^5D_3$, and $^7F_0 \rightarrow {}^5D_1$, respectively of Eu^{3+} ions. Overlapping of emission bands of $BaWO_4$ with the excitation bands of Tb^{3+} and Eu^{3+} reveal the apparent resonance type energy transfer between the matrix and the ions.[36] The red emission spectra of characteristic Eu^{3+} ions from $BaWO_4$:5Tb–5Eu, signifies the energy transfer between Tb^{3+} and Eu^{3+}. The red emission Eu^{3+} emission can be ascribe to the intrinsic $4f$–$4f$ ($^5D_4 \rightarrow {}^7F_{0-7}$) transitions, and to be precise, the emission peaks at 578, 592, 612, 654, and 702 nm are assigned to $^5D_4 \rightarrow {}^7F_0$, 5 $^5D_4 \rightarrow {}^7F_1$, $^5D_4 \rightarrow {}^7F_2$, $^5D_4 \rightarrow {}^7F_3$, and $^5D_4 \rightarrow {}^7F_4$ transitions of Eu^{3+}, respectively.[37]

PL spectra of $BaWO_4$:xTb nanofibers are shown in Fig. 6a. The PL spectrum consists of strong characteristic peaks of Tb^{3+} ions originate from $4f$–$4f$ transitions when excited by 247 nm wavelength source. The emission characteristic to the $BaWO_4$ matrix is completely disappeared on doping with Tb^{3+}, and the significant sharp $4f$–$4f$ green emissions of Tb^{3+} ions are evident at every concentration of Tb^{3+} ions. Therefore, the non-radiative energy transfer from the matrix to Tb^{3+} ions is evident in these nanofibers. The intensity of emission from Tb^{3+} ions are gradually decreased with Tb^{3+} concertation, and the most intense emission is observed from the nanofibers doped with 5 mol.% of Tb^{3+} ions. The reduction in Tb^{3+} emission intensity at higher concentrations above 15 mol.% could be attributed to Tb^{3+}–Tb^{3+} internal concentration quenching, during which the excitation energy is lost by the energy migration among the activator ions.

In the PL spectra of $BaWO_4$:5Tb–zEu nanofibers, as shown in Fig. 6b, strong emissions in the orange-red region is observed. As the Eu^{3+} concentration is increased, the red emission intensity increases monotonically; at the same time, the intensity of Tb^{3+} ions is drastically decreased. The emission from Tb^{3+} ions is completely disappeared when the Eu^{3+} concentration is 5%. In both 1% and 3% Eu^{3+} doped $BaWO_4$ nanofibers, the characteristic emission from both Tb^{3+} and Eu^{3+} ions are dominant. In all the instances, the intensity of the Eu^{3+} emission line at 616 nm is significant in comparison to the emission at 591 nm. The PL emission at 616 nm, electric dipole transition of Eu^{3+} ions, is very sensitive to the local environment and the symmetry of the crystal field. However, the emission at 593 nm is not influenced well by the crystal field, which is a magnetic dipole transition of Eu^{3+}.[38] Therefore, Eu^{3+} ions are in an asymmetric environment without inversion symmetry, meaning, in the $BaWO_4$ host matrix, RE^{3+} ions replace Ba^{2+} ions with Tetragonal symmetry (S4 point symmetry). Moreover, the electronic densities of RE^{3+} and Ba^{2+} and their coordination numbers are analogous, despite the lower symmetry due to the valence mismatch between RE^{3+} and Ba^{2+} ions and the resulting charge compensating defects.[39]

Table 2. CIE Coordinates calculated from the PL spectra of $BaWO_4$ nanofiber phosphors

Sl. No	Sample composition	CIE (x)	CIE (y)
1	$BaWO_4$	0.1569	0.1257
2	$BaWO_4$:5Tb	0.2849	0.5118
3	$BaWO_4$:10Tb	0.2479	0.5102
4	$BaWO_4$:15Tb	0.3498	0.4975
5	$BaWO_4$:20Tb	0.3154	0.3615
6	$BaWO_4$:25Tb	0.2507	0.3101
	$BaWO_4$:5Tb–0.5Eu	0.3182	0.4976
8	$BaWO_4$:5Tb–1.0Eu	0.3478	0.4103
9	$BaWO_4$:5Tb–3.0Eu	0.3683	0.3556
10	$BaWO_4$:5Tb–5.0Eu	0.6335	0.3498

The CIE diagrams and the corresponding coordinates of the nanofibers when excited by 247 nm source are presented in Fig. S4 and Table 2, respectively. The emission from the nanowires is scattered in the blue, green, and red regions. White light is also produced in the case of nanofibers doped with Tb^{3+} and Eu^{3+}. Therefore, the color of the emission can be controlled precisely by adding the appropriate amount of the dopant.

Cathodoluminescence characteristics

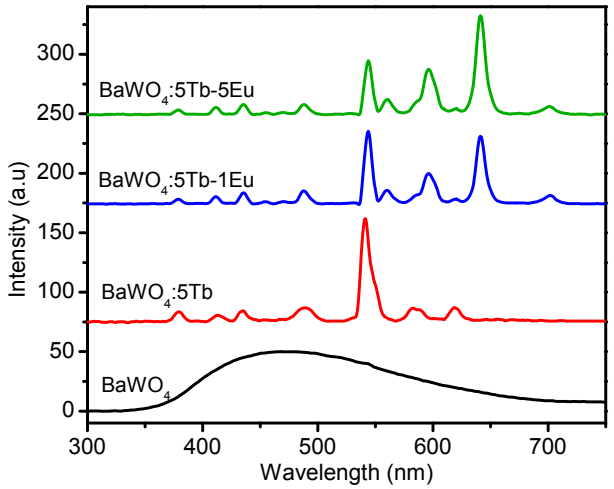

Fig. 7. Cathodoluminescent emission of pure and RE^{3+} doped $BaWO_4$ nanofibers.

The cathodoluminescence (CL) spectra of the pure and doped $BaWO_4$ nanofibers is recorded under 10 kV and 100 nA electron beam, aimed to simulate the response of the nanofibers towards high energy radiation. The characteristic CL emission spectra are shown in Fig. 7. The pure $BaWO_4$ nanofibers emit a broad visible spectrum in the wide range of 300–750 nm (majorly blue and green bands) when excited by an electron beam. Which is similar to the PL emission characteristics. The CL emission in the pure lattice is originated by the propagation of ionization initiated by the fast–primary electrons. The

ultraviolet and visible light usually excite the activator directly; the fast electrons as high-energy particles always excite the host lattice.[40] Similar to other isomorphous scheelite structures, the CL emission spectra of $BaWO_4$ is akin to electronic transitions that take place within the $[WO_4]^{2-}$ ions, which is evident in the PL spectrum of pure $BaWO_4$. According to crystal field theory, for $[WO_4]^{2-}$ ligands with T_d symmetry, the ground state is $^1A_1$, and there are four singlet excited states $^1A(^1T_1)$, $^1E(^1T_1)$, $^1E(^1T_2)$, and $^1B(^1T_2)$. The blue emission band is an intrinsic emission due to an electron transition $^1B(^1T_2)\rightarrow{}^1A_1$ of the $[WO_4]^{2-}$ complex ions, and the green emission band is due to the WO_3 defects that are associated with oxygen vacancies.[41]

In the CL spectra of $BaWO_4$:5Tb and $BaWO_4$:5Tb−(1,5)Eu nanofibers, the emission peaks originated from the $BaWO_4$ lattices are entirely disappeared. The CL spectra of $BaWO_4$:5Tb nanofibers comprise the most intense emission lines at 544 nm, which is due to the Tb^{3+} ions as in the PL spectra. Since the emission from the $BaWO_4$ lattices is completely disappeared in the CL spectra, the energy transfer from the host lattice to Tb^{3+} ions are recognized. All the possible transitions of Tb^{3+} are visible in the CL spectra, which does not appear in the PL spectra. The several small peaks in the blue region <450 nm is due to $^5D_3\rightarrow{}^7F_J$ (J =6, 5, 4, 3) transitions and the peaks in green region >450 are due to $^5D_4\rightarrow{}^7F_J$ (J = 6, 5, 4, 3) transitions of Tb^{3+} ions.[40] The emission band from Eu^{3+} ions are appeared in $BaWO_4$:5Tb−(1,5)Eu nanofibers. The emission lines characteristic to Tb^{3+} ions is present in all the CL spectra of the doped nanofibers. The emission intensity from Eu^{3+} ions $BaWO_4$:5Tb−(1,5)Eu nanofibers are remarkable, which is dependent on the Eu^{3+} concentration. The emission from Tb^{3+}/Eu^{3+} doped nanofibers, the emission is independent of the emission from the Tb^{3+} ions. The simultaneous emission observed from Tb^{3+} and Eu^{3+} ions are possibly due to the contemporary energy transfer to these ions from the lattice. Therefore, in the case of doped nanofibers, as the secondary electrons excite the host lattice and create many electron–hole pairs, leading to the formation of bound excitons. As no luminescence from bound exciton recombination is observed, these excitons, if formed, decay non-radiatively through a resonant or quasi-resonant transfer to the 4*f* shell of Eu^{3+} and/or Tb^{3+} ions and give their characteristic emission.[42]

Photoluminescence sensitivity towards 2-nitrotoluene and H_2O_2

The PL response of $BaWO_4$ nanofibers upon exposure to the model explosive taggants 2-nitrotoluene and H_2O_2 is investigated by dispersing the nanofibers in water. The sensing performance of representative RE^{3+} doped $BaWO_4$ nanofibers dispersed in water is tested by recording the fluorescent spectra in the presence of different concentrations of 2-nitrotoluene, as

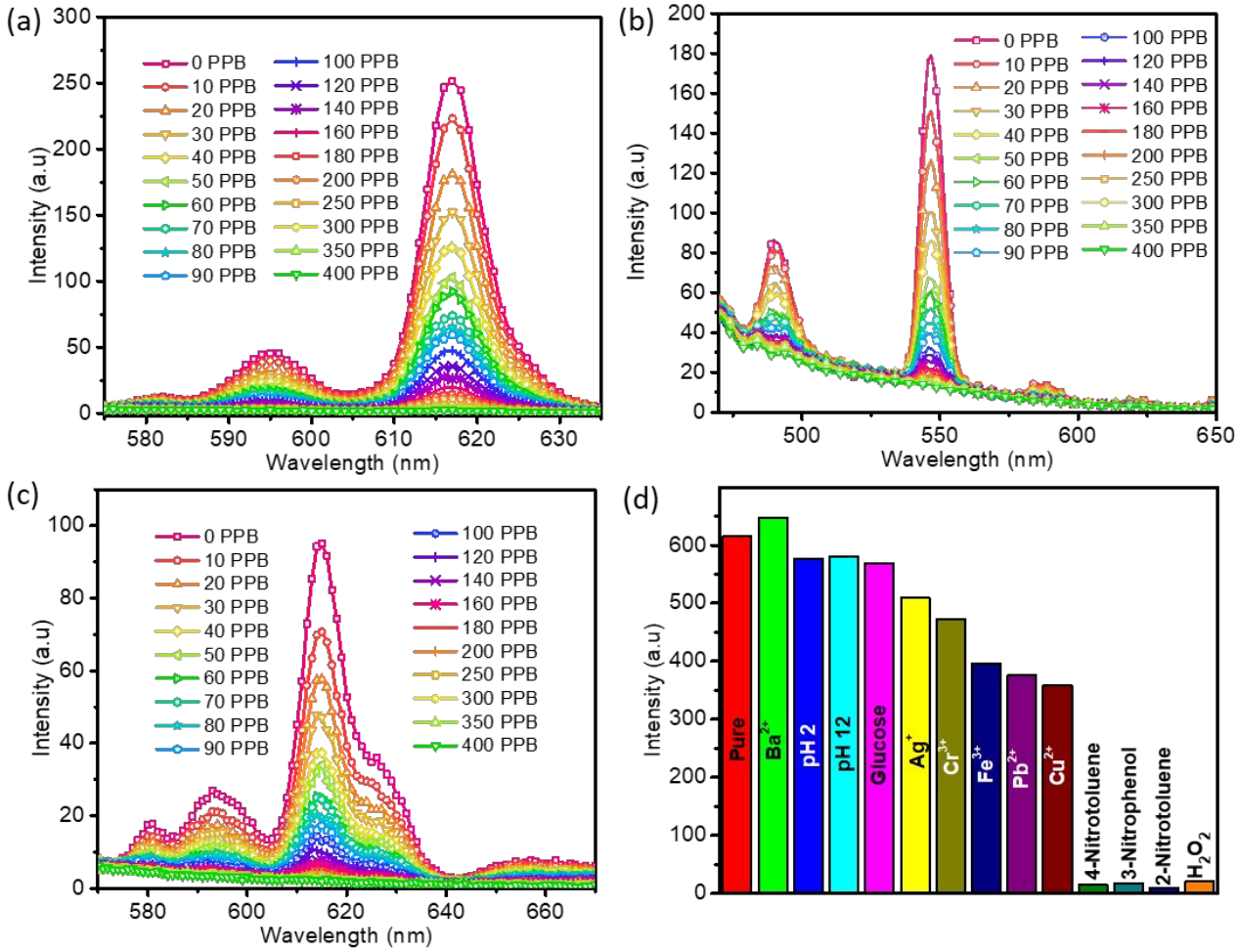

Fig. 8. PL response of (a) $BaWO_4$:5Tb−5Eu, (b) $BaWO_4$:5Tb, (c) $BaWO_4$:5Eu nanofibers dispersed in water towards 2-nitrotoluene concentration, and (c) selectivity of $BaWO_4$:5Tb−5Eu nanofiber dispersion in water towards 2-nitrotoluene and H_2O_2.

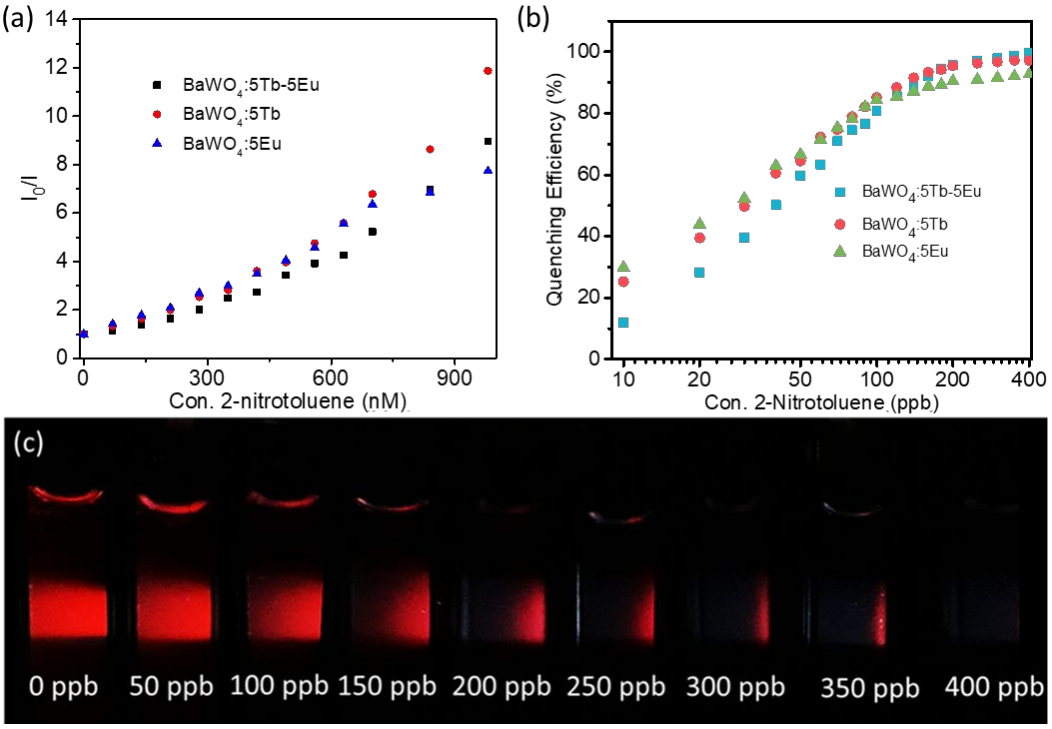

Fig. 9. (a) Stern–Volmer plots, and (b) quenching efficiency, of RE^{3+} doped $BaWO_4$ nanofibers and (c) extinction of luminescence with increasing concentration of 2-nitrotoluene for nanofibers dispersed in water.

shown in Fig. 8a–c. The PL spectra of nanofiber dispersions in the presence of different concentrations of 2-nitrotoluene ranging from 10 ppb to 400 ppb, clearly show a change in the fluorescence of RE^{3+} doped $BaWO_4$ nanofibers concerning 2-nitrotoluene concentration. The quenching of the luminescent emission in the presence of 2-nitrotoluene in few parts per billion is rapid. The intensity of all RE^{3+} emission bands is decreased simultaneously in the presence of 2-nitrotoluene, when excited by 247 nm source. The presence of *2*–nitrotoluene can be quantified for concentrations between 10–400 ppb. Additionally, the selectivity of the sensory materials was tested with glucose, Fe^{3+}, Cu^{2+}, Ba^{2+}, Ag^{+}, Pb^{2+}, Cr^{2+}, and pH, as shown in Fig. 8d and the corresponding PL spectra is shown in Fig. S5. The sensitivity towards other nitroaromatic compounds are confirmed using 4-nitrotoluene and *3*-nitrophenol as the representative analytes. Their addition up to 1000 ppm to the $BaWO_4$:5Tb–5Eu dispersion leads to insignificant modifications to the luminescence intensity, whereas the addition 400 ppb of 2-nitrotoluene and 1000 ppb of H_2O_2 leads to a >95% decrease. The excellent selectivity of the sensor nanofibers towards 2-nitrotoluene and H_2O_2, as compared to other disturbants, highlights RE^{3+} doped $BaWO_4$ nanofibers as a promising fluorescent probe for the detection of explosives even at nM concentrations.The mechanism involved in the detection process can be related to the quenching of the RE^{3+} emission.

In general, nitro compounds are electron-deficient, and quenching of fluorescence occurs via photoinduced donor-acceptor electron transfer mechanism.[2d] Where RE^{3+} ions are donors and 2-nitrotoluene molecules are acceptors, which does not exhibit any luminescence. $BaWO_4$ crystallizes with $[WO_4]^{2-}$ tetrahedrons on the surface covering the Ba^{2+} ions, as a result, the surface of $BaWO_4$ exhibit a partial negative (δ^-) charge as in the case of $CaWO_4$ due to high surface density of active oxygen

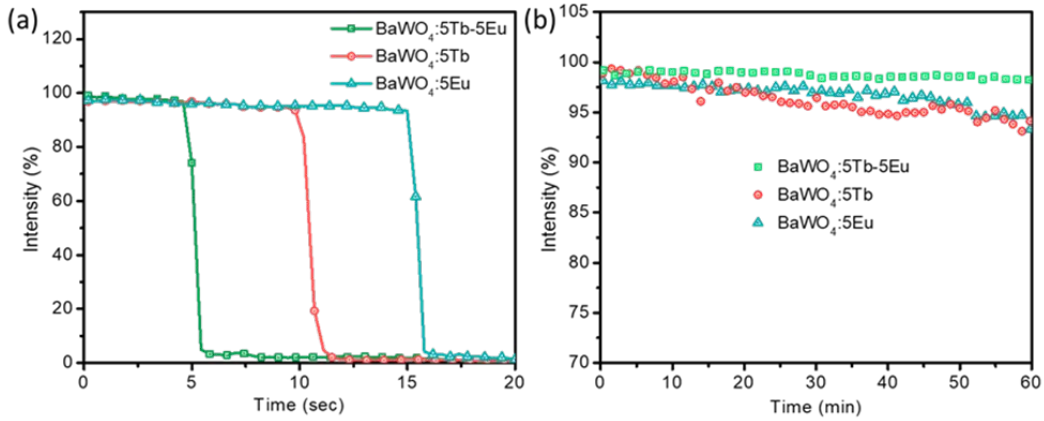

Fig. 10. (a) The response time for PL quenching in the presence of 2-nitrotoluene and (b) photobleaching of RE^{3+} doped $BaWO_4$ nanofiber dispersions in water.

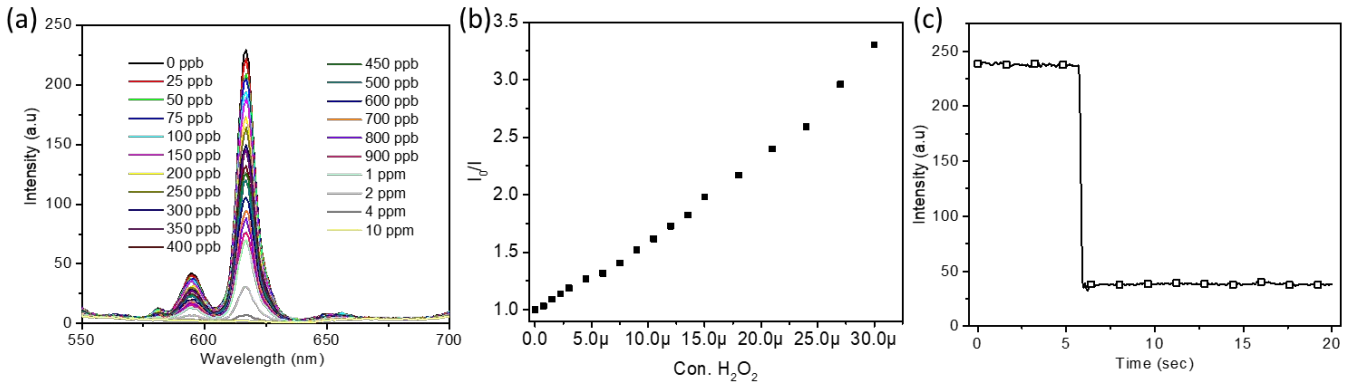

Fig. 11. (a) PL response of $BaWO_4$:5Tb–5Eu nanofiber dispersion in water towards H_2O_2 concentration, (b) Stern–Volmer plot, and (c) the response time for PL quenching in the presence of H_2O_2.

atoms.[43,44] The crystal structure of $BaWO_4$ is shown in Fig. S6. Importantly, $[WO_4]^{2-}$ is the anion of strong tungstic acid with a susceptibility towards positive charges. The super adsorption of cationic dyes on $BaWO_4$ nanostructures is corroborated to the electrostatic interaction between dye and the partial negative charges on the surface of $BaWO_4$.[45] Apparently, $BaWO_4$ nanofibers can be a super adsorbent towards 2-nitrotoluene through the electrostatic bonding between the partial negative charges of the $BaWO_4$ surface and the partial positive (δ^+) charge of the benzene rings of 2-nitrotoluene (formed by the electron pulling of N^+ ions). This interaction is evident in the FTIR absorbance spectra (Fig. S7a&b) of $BaWO_4$:5Tb–5Eu nanofibers in the presence and absence of 2-nitrotoluene. The peak originated from $[WO_4]^{2-}$ ligand of $BaWO_4$ is shifted to lower wavenumbers in the presence of 2-nitrotoluene, which can be ascribed to the hindrance in the vibration of $[WO_4]^{2-}$ ligand induced by 2-nitrotoluene, which is obvious from Fig. S7b. The subsequent changes in the peak position of the benzene rings of 2-nitrotoluene is also observed vice versa in the FTIR spectrum of $BaWO_4$ in the presence of 2-nitrotoluene.

Additionally, on comparing the UV absorption spectra of the analytes and the emission spectra of the pure $BaWO_4$, as in Fig. S8, the UV absorption of the nitroaromatic analytes is overlapping with the emission spectra of the pure $BaWO_4$ nanofibers. The UV spectra of the nanofibers shown in Fig. S9, does not reveal any significant absorption bands of RE^{3+} ions, though the PLE spectra (Fig. 5) reveal the weak absorbance of the RE^{3+} ions overlapping the emission spectra of the $BaWO_4$ lattice. Apparently, one can conclude that there is a competition between the RE^{3+} ions and the analytes to receive the energy non-radiatively from the excited lattice. Therefore, the anticipated donor-acceptor type energy transfer is prone between the lattice and the nitro-aromatic compounds than the RE^{3+} ions in the presence of nitro-aromaticsThe LUMO (lowest unoccupied molecular orbital) energy levels of 2,4,6–trinitrotoluene (TNT) and 2,4–dinitrotoluene (DNT) is smaller than 2-nitrotoluene; therefore, one can expect an easier electron transfer from donor to TNT and DNT than 2-nitrotoluene, hence an improved sensitivity towards TNT and DNT is expected.[9,46] A schematic of the energy-transfer quenching mechanism in the absence and presence of 2–nitrotoluene is presented in Fig. S10. A slightly higher quenching percentage for $BaWO_4$:5Tb–5Eu as compared to $BaWO_4$:5Tb and $BaWO_4$:5Eu is observed at room temperature besides the high-intensity emission and relative quantum yield from the $BaWO_4$:5Tb–5Eu nanofibers.

The Stern–Volmer plots of the relative luminescent intensity (I_0/I) versus the concentration of *2*-nitrotoluene are shown in Fig. 9a. The Stern–Volmer plots of $BaWO_4$:5Tb–5Eu, $BaWO_4$:5Tb, and $BaWO_4$:5Eu can be fitted well to the exponential equations $1.67e^{1.80\times10^6[NT]}-0.719$, $3.88\ e^{1.33\times10^6[NT]}-3.15$, and $2.45e^{1.62\times10^6[NT]}-1.36$, respectively. The Stern–Volmer curves are nonlinear as compared to the typical linear ones may be a result of simultaneous static and dynamic quenching.[47]

The quenching coefficients are calculated using the equation,[97]

$$I_0/I = (K_D[\mathrm{NT}]+1)(K_s[\mathrm{NT}]+1) \quad (1)$$

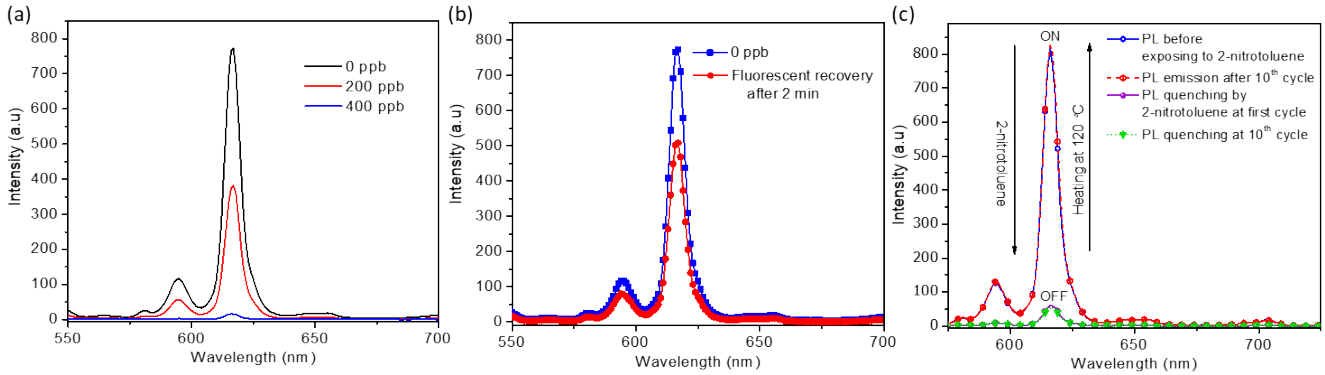

Fig. 12. (a) PL response of $BaWO_4$:5Tb–5Eu nanofibers in solid-state to 2-nitrotoluene, (b) sensor recovery in atmospheric conditions, and (c) sensor response during the repeated cycles.

Where I_0 and I are the fluorescence intensity in the absence and presence of 2-nitrotoluene, K_D is the dynamic quenching constant, K_S is the static quenching constant and [NT] is the concentration of 2-nitrotoluene. The calculated quenching constants are $K_D = K_S = 1.73\times10^6$ and 2.1×10^6, and 2.2×10^6 $L\cdot mol^{-1}$, $BaWO_4$:5Tb−5Eu, $BaWO_4$:5Tb, and $BaWO_4$:5Eu nanofibers, respectively, in the low-concentration range.

Table 3. Comparison of RE^{3+} doped $BaWO_4$ nanofibers with luminescent explosive probes reported in literature.

Sl. No	Material	Quenching constant ($L\cdot mol^{-1}$)	Limit of detection (μM)	Ref
1	N-doped graphene quantum dots	-	0.92	48
2	Cd(II) MOF	7.4×10^4	-	12b
3	Dansyl conjugated tripodal AIEEgen	3.79×10^7	0.001	49
4	Cd based MOF	6.56×10^4	2	50
5	Lysozyme capped CdS quantum dots	3.28×10^4	0.1	51
6	Cu based MOF	1.6×10^4	3.2	26
7	Zr(IV) MOF	2.9×10^4	-	52
8	*p*-phenylenevinylene	8.53×10^4	0.035	53
9	Zn(II) MOF	1.09×10^4	-	12a
10	Zn(II) MOF	4.86×10^3	-	54
11	$BaWO_4$:5Eu-5Tb nanofibers	1.73×10^6	0.035	Present Work
12	CdSe quantum dots	1.31×10^5	0.021	27
13	Carbon dots	5.99×10^4	0.2	55
14	Carbon quantum dots functionalized with amines	2.31×10^4	2.57	56
15	Indium based MOF	1.65×10^5	0.32	57
16	Cd based MOF	5.42×10^4	8	58

The dramatically high quenching constants reveals the very high sensitivity of the nanofibers towards the detection of explosive taggants. The detection limit (LOD) was calculated according to the equation: $LOD = 3S_0/K$, where S_0 is the standard deviation of blank RE^{3+} doped $BaWO_4$ nanofiber emission (n = 10), and K is the slope of the calibration graph.[27] The LOD is estimated in the range of 35–45 nM for the three different nanofibers. On comparing the literature data available for the detection of nitro-compounds using various luminescent materials, the performance of inorganic RE^{3+} doped $BaWO_4$ nanofibers is exceeding most of them, as listed in Table 3.

The quenching efficiency ($QE = (I_0 - I)/I_0 \times 100$) curves of the nanofibers are shown in Fig. 9b. The increase in the concentration of 2-nitrotoluene enhance quenching efficiency; however, a steady increase in efficiency is observed at lower concentrations of 2-nitrotoluene, which has a linear relationship with ln[NT]. The quenching phenomenon can also be observed to the naked eye under 247 nm UV excitation, as an annihilation of the red luminescence with the stepwise addition of 2-nitrotoluene as in Fig. 9c. In the presence of 2-nitrotoluene, the luminescence intensity of the RE^{3+} doped $BaWO_4$ nanofibers is drastically reduced and the response time is measured in the presence of 400 ppb 2-nitrotoluene, shown in Fig. 10a. The results show that all the nanofibers exhibit a similar response time, which is less than one second. The photostability of the $BaWO_4$ nanofibers is measured under irradiation of 247 nm for 60 min, Fig. 10b. For $BaWO_4$:5Tb−5Eu and $BaWO_4$:5Eu nanofibers, the intensity at 617 nm is monitored and for $BaWO_4$:Tb nanofibers, the intensity at 545 nm emission is monitored to study the effect of photobleaching. Photobleaching is negligible in all the fibers. However, high stability is observed in the case of $BaWO_4$:5Tb−5Eu nanofibers. The high stability of these nanowires under UV light can increase the lifespan of this material as a sensor.[59]

The fluorescent quenching characteristics using $BaWO_4$:5Tb−5Eu nanofibers as the representative nanofibers towards H_2O_2 is also studied, as shown in Fig. 11a. A gradual reduction in the luminescent intensity is observed in the presence of different concentrations of H_2O_2. From the Stern−Volmer plot, Fig. 11b, the calculated quenching constants in the low-concentration range are $K_D = K_S = 2.71\times10^4$ $L\cdot mol^{-1}$. The response time observed here (Fig. 11c) is less than one second, which is rapid as compared to many other sensors reported in the literature. The LOD of $BaWO_4$:5Tb−5Eu nanofibers towards H_2O_2 is 4 μM. The Stern−Volmer constants and the LOD of the $BaWO_4$:5Tb−5Eu nanofibers are at par with the performance of the scheelite structured $EuVO_4$ nanoparticles with the corresponding values 10^5 $L\cdot mol^{-1}$ and 1.5 μM, respectively,[6] and nanoparticles surface modified with luminescent molecules.[60] The performance of the $BaWO_4$ nanofibers towards the sensing of H_2O_2 is superior to $BaGeF_6$ and $BaSiF_6$ nanowires reported in our previous study.[61] Importantly, the nanofibers are more practical in such studies as the recovery of the nanofibers is more convenient than the nanoparticles for repeated use.

The sensitivity of the $BaWO_4$:5Tb−5Eu nanofibers in the solid-state to the explosive vapors are also studied after pasting the nanofibers on a glass slide. The emission from the nanofibers pasted on the glass slide is recorded before and after exposing the nanofibers to a known quantity of 2-nitrotoluene vapors created by heating in a petri dish as shown in Fig. S11. The characteristic emission from the nanofibers dropped drastically after exposing the nanofibers to the explosive vapors, akin to that in the solution, which is shown in Fig. 12a. The reversibility of the nanofibers as explosive sensors are performed using 2-nitrotoluene as the model analyte. More than 60% of the luminescent emission is recovered after 2 min under normal atmospheric conditions after exposing the nanofibers to 400 ppb 2-nitrotoluene, as shown in Fig. 12b. However, the luminescence of the nanofibers is retained completely after heating at 120 °C for 10 min. The process is repeated up to 10 cycles, and the sensory response is retained as fresh nanofibers (Fig. 12c), revealing the high reversibility of these nanofibers, unlike many other disposable organic luminescent sensors. The stability of PL emission from the nanofibers in the solid state under prolonged UV excitation is assessed, which is shown in Fig. S12. The emission from the solid nanofibers is stable under UV light up to 60 minutes. Therefore, RE^{3+} doped $BaWO_4$ nanofibers can be used as a simple, stable, reusable, versatile, and efficient sensor for the simultaneous detection of peroxide and nitro- organic explosives.

Conclusions

High-aspect-ratio pure and rare-earth-doped $BaWO_4$ nanofibers were successfully fabricated through sol-gel assisted electrospinning method. The nanofibers exhibited visible photoluminescence and cathodoluminescence emissions when codoped with varying mol.% of Tb^{3+}, and Eu^{3+} rare–earth ions. The XRD analysis revealed the crystalline nature of the nanofibers with tetragonal structure, and the structure is not affected by the rare–earth dopants. The PL emission monitored when excited by 247 nm source can be tailored by adjusting the amount of Tb^{3+} and Eu^{3+} ions. The intense blue CL emission from pure $BaWO_4$ nanofibers and green and red emissions from Tb^{3+} and Eu^{3+} doped nanofibers are observed, which is characteristic of these ions. The visible PL emissions from the RE^{3+} doped $BaWO_4$ nanofibers are highly sensitive to 2-nitrotoluene and H_2O_2 with quenching coefficients in the order of 10^6 and 10^4 $L{\cdot}mol^{-1}$, respectively to 2-nitrotoluene and H_2O_2. The limit of detections of the nanofibers towards 2-nitrotoluene and H_2O_2 are 0.035–0.045 µM and 1 µM, respectively. The performance of the RE^{3+} doped $BaWO_4$ nanofibers are better than most of the organic materials reported for the detection of nitro-explosives and at par with the scheelite structured $EuVO_4$ nanoparticles for H_2O_2 sensing. The rapid response, stability, and reusability identify this nanofiber material as a promising commercial sensor for highly selective and sensitive detection of explosives of two different origins.

Conflicts of interest

There are no conflicts to declare.

Acknowledgments

The authors would like to thank Army Research Office (ARO), Department of Defense (DoD), for research funding, Contract No. W911NF1810469. The instrumentation was supported by the U.S. DoD grants W911NF-14-1-0060, W911NF-15-1-0566 and W911NF-09-1-0011, and NSF MRI Program DMR 1626376. Use of the Center for Nanoscale Materials, an Office of Science user facility, was supported by the U.S. Department of Energy, Office of Science, Office of Basic Energy Sciences, under Contract No. DE-AC02-06CH11357.

References

1 (a) X. Zhao and J. Yinon, *J. Chromatogr. A*, 2002, **946**, 125–132; (b) M. Berg, J. Bolotin and T. B. Hofstetter, *Anal. Chem.*, 2007, **79**, 2386–2393; (c) S. Babaee and A. Beiraghi, *Anal. Chim. Acta*, 2010, **662**, 9–13; (d) M. Najarro, M. E. D. Morris, M. E. Staymates, R. Fletcher and G. Gillen, *Analyst*, 2012, **137**, 2614–2622; (e) P. Sulzer, F. Petersson, B. Agarwal, K. H. Becker, S. Jürschik, T. D. Märk, D. Perry, P. Watts and C. A. Mayhew, *Anal. Chem.*, 2012, **84**, 4161–4166; (f) S. Guo, D. Wen, Y. Zhai, S. Dong and E. Wang, *ACS Nano*, 2010, **4**, 3959–3968; (g) M. Y. Ho, N. D'Souza and P. Migliorato, *Anal. Chem.*, 2012, **84**, 4245–4247; (h) H.-X. Zhang, A.-M. Cao, J.-S. Hu, L.-J. Wan and S.-T. Lee, *Anal. Chem.*, 2006, **78**, 1967–1971; (i) M. Riskin, R. Tel-Vered and I. Willner, *Adv. Mater.*, 2010, **22**, 1387–1391; (j) S. S. R. Dasary, A. K. Singh, D. Senapati, H. Yu and P. C. Ray, *J. Am. Chem. Soc.*, 2009, **131**, 13806–13812; (k) Y. Ma, H. Li, S. Peng and L. Wang, *Anal. Chem.*, 2012, **84**, 8415–8421.

2 (a) M. E. Germain and M. J. Knapp, *Chem. Soc. Rev.*, 2009, **38**, 2543–2555; (b) H. Sohn, M. J. Sailor, D. Magde and W. C. Trogler, *J. Am. Chem. Soc.*, 2003, **125**, 3821–3830; (c) J. V. Goodpaster and V. L. McGuffin, *Anal. Chem.*, 2001, **73**, 2004–2011; (d) X. Sun, Y. Wang and Y. Lei, *Chem. Soc. Rev.*, 2015, **44**, 8019–8061; (e) R. C. Stringer, S. Gangopadhyay and S. A. Grant, *Anal. Chem.*, 2010, **82**, 4015–4019; (f) B. Gole, A. K. Bar and P. S. Mukherjee, *Chem. Commun.*, 2011, **47**, 12137–12139; (g) D. Li, J. Liu, R. T. K. Kwok, Z. Liang, B. Z. Tang and J. Yu, *Chem. Commun.*, 2012, **48**, 7167–7169; (h) N. Venkatramaiah, S. Kumar and S. Patil, *Chem. Commun.*, 2012, **48**, 5007–5009.

3 (a) Y. Xia, L. Song and C. Zhu, *Anal. Chem*., 2011, **83**, 1401–1407; (b) D. Haldar, D. Dinda and S. K. Saha, *J. Mater. Chem. C*, 2016, **4**, 6321–6326; (c) K. Zhang, H. Zhou, Q. Mei, S. Wang, G. Guan, R. Liu, J. Zhang and Z. Zhang, *J. Am. Chem. Soc.*, 2011, **133**, 8424–8427; (d) W. J. Peveler, A. Roldan, N. Hollingsworth, M. J. Porter and I. P. Parkin, *ACS Nano*, 2016, **10**, 1139–1146.

4 (a) D. Banerjee, Z. Hu and J. Li, *Dalton Trans.*, 2014, **43**, 10668–10685; (b) Y. Cui, Y. Yue, G. Qian and B. Chen, *Chem. Rev.*, 2012, **112**, 1126–1162.

5 L. Senesac and T. G. Thundat, *Mater. Today*, 2008, **11**, 28–36.

6 N. Duée, C. Ambard, F. Pereira, D. Portehault, B. Viana, K. Vallé, D. Autissier and C. Sanchez, *Chem. Mater.*, 2015, **27**, 5198–5205.

7 (a) R. S. Aparna, J. S. Anjali Devi, R. R. Anjana, J. Nebu and S. George, *Sens. Actuators B Chem.*, 2019, **291**, 298–305; (b) Q. Wang, D. J. Liu, L. L. Cui, X.-L. Hu, X.-L. Wang and Z.-M. Su, *New J. Chem.*, 2019, **43**, 963–969; (c) H. Turhan, E. Tukenmez, B. Karagoz and N. Bicak, *Talanta*, 2018, **179**, 107–114; (d) W. Wu, N. Shi, J. Zhang, X. Wu, T. Wang, L. Yang, R. Yang, C. Ou, W. Xue, X. Feng, L. Xie and W. Huang, *J. Mater. Chem. A*, 2018, **6**, 18543–18550.

8 M. S. Meaney and V. L. McGuffin, *Anal. Chim. Acta*, 2008, 610, 57-67.

9 S. S. Nagarkar, B. Joarder, A. K. Chaudhari, S. Mukherjee and S. K. Ghosh, *Angew. Chem. Int. Ed*., 2013, **52**, 2881- 2885

10 Y. Xu, B. Li, W. Li, J. Zhao, S. Sun and Y. Pang, *Chem. Commun*., 2013, 49, 4764-4766.

11 A. Tournebize, P. Wong-Wah-Chung, S. Thérias, P.-O. Bussière, A. Rivaton, T. Caron, F. Serein-Spirau, J.-P. Lère-Porte, P. Montméat and J.-L. Gardette, *Polym. Degrad. Stab.*, 2012, **97**, 1355–1365.

12 (a) X.-X. Wu, H.-R. Fu, M.-L. Han, Z. Zhou and L.-F. Ma, *Cryst. Growth Des.*, 2017, **17**, 6041–6048; (b) L. Yang, X. Li, C. Qin, K.-Z. Shao and Z.-M. Su, *CrystEngComm*, 2016, **18**, 4765–4771.

13 (a) Z. Hou, P. Yang, C. Li, L. Wang, H. Lian, Z. Quan and J. Lin, *Chem. Mater.*, 2008, **20**, 6686–6696; (b) H. Farsi, Z. Barzgari and S. Z. Askari, *Res. Chem. Intermed.*, 2015, **41**, 5463–5474; (c) A. Sahmi, K. Bensadok and M. Trari, *J. Photochem. Photobiol. Chem.*, 2017, **349**, 36–41; (d) M. Li, Q. Meng, S. Li, F. Li, Q. Zhu, B.-N. Kim and J.-G. Li, *Ceram. Int.*, 2019, **45**, 10746–10755; (e) Y. Zhang, R. Fan, Q. Zhang, Y. Chen, O. Sharifi, D. Leszczynska, R. Zhang and Q. Dai, *Mater. Res. Bull.*, 2019, **110**, 169–173.

14 D. Wang, K. Pan, Y. Qu, G. Wang, X. Yang and D. Wang, *ACS Appl. Nano Mater.*, 2018, **1**, 4762–4770.

15 (a) L. S. Cavalcante, J. C. Sczancoski, N. C. Batista, E. Longo, J. A. Varela and M. O. Orlandi, *Adv. Powder Technol.*, 2013, **24**, 344–353; (b) M. J. Kim, H. Park and H. J. Kim, *J. Korean Phys. Soc.*, 2016, **69**, 1130–1134; (c) M. Moszyński, M. Balcerzyk, W. Czarnacki, A. Nassalski, T. Szczęśniak, H. Kraus, V. B. Mikhailik and I. M. Solskii, *Nucl. Instrum. Methods Phys. Res. Sect. Accel.*

Spectrometers Detect. Assoc. Equip., 2005, **553**, 578–591; (d) Z. Shan, Y. Wang, H. Ding and F. Huang, *J. Mol. Catal. Chem.*, 2009, **302**, 54–58; (e) D. Spassky, V. Mikhailin, M. Nazarov, M. N. Ahmad-Fauzi and A. Zhbanov, *J. Lumin.*, 2012, **132**, 2753–2762.

16 P. Černý and H. Jelínková, *Opt. Lett.*, 2002, **27**, 360–362.

17 Y. Wang, Y. Qu, K. Pan, G. Wang and Y. Li, *Chem. Commun.*, 2016, **52**, 11124–11126.

18 (a) S. Cho, *Appl. Surf. Sci.*, 2018, **432**, 202–206; (b) H. Wu, J. Yang, X. Wang, S. Gan and L. Li, *Solid State Sci.*, 2018, **79**, 85–92; (c) S. Vidya, S. Solomon and J. K. Thomas, *Adv. Condens. Matter Phys.*, 2013, 409620, DOI:10.1155/2013/409620; (d) V. Caracciolo, F. Cappella, R. Cerulli, A. D. Marco, M. Laubenstein, S. S. Nagorny, O. E. Safonova and V. N. Shlegel, *Nucl. Instrum. Methods Phys. Res. Sect. Accel. Spectrometers Detect. Assoc. Equip.*, 2018, **901**, 150–155; (e) Lorena. D. S. Alencar, A. Mesquita, C. A. C. Feitosa, R. Balzer, L. F. D. Probst, D. C. Batalha, M. G. Rosmaninho, H. V. Fajardo and M. I. B. Bernardi, *Ceram. Int.*, 2017, **43**, 4462–4469; (f) A. Sahmi, S. Omeiri, K. Bensadok and M. Trari, *Mater. Sci. Semicond. Process.*, 2019, **91**, 108–114; (g) L. I. Ivleva, I. S. Voronina, P. A. Lykov, L. Yu. Berezovskaya and V. V. Osiko, *J. Cryst. Growth*, 2007, **304**, 108–113.

19 (a) F.-Q. Dong, Q.-S. Wu and Y.-P. Ding, *J. Alloys Compd.*, 2009, **476**, 571–574; (b) K. Kawashima, J.-H. Kim, I. Cheng, K. Yubuta, K. Shin, Y. Liu, J. Lin, G. Henkelman and C. B. Mullins, *Cryst. Growth Des.*, 2018, **18**, 5301–5310; (c) H. Shi, L. Qi, J. Ma and H. Cheng, *Chem. Commun.*, 2002, **48**, 1704–1705; (d) H. Shi, L. Qi, J. Ma and H. Cheng, *J. Am. Chem. Soc.*, 2003, **125**, 3450–3451; (e) Z. Luo, H. Li, J. Xia, W. Zhu, J. Guo and B. Zhang, *Mater. Lett.*, 2007, **61**, 1845–1848; (f) X. Zhao, T. Li, Y. Xi, D. H. L. Ng and J. Yu, *Cryst. Growth Des.*, 2006, **6**, 2210–2213; (g) L. Zhang, J.-S. Dai, L. Lian and Y. Liu, *Superlattices Microstruct.*, 2013, **54**, 87–95.

20 G. George and Z. Luo *Curr. Nanosci.*, 2019, **15**, DOI:10.2174/1573413715666190112121113.

21 (a) X. Wang, Y.-G. Kim, C. Drew, B.-C. Ku, J. Kumar and L. A. Samuelson, *Nano Lett.*, 2004, **4**, 331–334; (b) J. Yao, P. Ji, B. Wang, H. Wang and S. Chen, *Sensors and Actuators B: Chemical*, 2018, **254**, 110–119; (c) X. Wang, Y. Wang, Y. Shan, M. Jiang, M. Gong, X. Jin, X. Wang and J. Cheng, *Talanta*, 2018, **187**, 179–187.

22 (a) H. Liu, J. B. Edel, L. M. Bellan and H. G. Craighead, *Small*, 2006, **2**, 495–499; (b) F. Gu, H. Yu, P. Wang, Z. Yang and L. Tong, *ACS Nano*, 2010, **4**, 5332–5338.

23 *U.S. Pat.*, US20100177518A1, 2010.

24 S. Pagliara, A. Camposeo, A. Polini, R. Cingolani and D. Pisignano, *Lab Chip*, 2009, **9**, 2851–2856.

25 (a) F. Quochi, F. Cordella, A. Mura, G. Bongiovanni, F. Balzer and H.-G. Rubahn, *J. Phys. Chem. B*, 2005, **109**, 21690–21693; (b) A. Camposeo, F. D. Benedetto, R. Stabile, A. A. R. Neves, R. Cingolani and D. Pisignano, *Small*, 2009, **5**, 562–566; (c) A. Camposeo, L. Persano and D. Pisignano, *Macromol. Mater. Eng.*, **298**, 487–503.

26 M. Jurcic, W. J. Peveler, C. N. Savory, D.-K. Bučar, A. J. Kenyon, D. O. Scanlon and I. P. Parkin, *ACS Appl. Mater. Interfaces*, 2019, **11**, 11618–11626.

27 K.-Y. Yi, *Forensic Sci. Int.*, 2016, **259**, 101–105.

28 C. Peniche, D. Zaldívar, M. Pazos, S. Páz, A. Bulay and J. S. Román, *J. Appl. Polym. Sci.*, 1993, **50**, 485–493.

29 R. Chandrasekar, L. Zhang, J. Y. Howe, N. E. Hedin, Y. Zhang and H. Fong, *J. Mater. Sci.*, 2009, **44**, 1198.

30 B. Mistry, *Handbook of Spectroscopic Data: Chemistry - UV,IR,PMR,CNMR and Mass Spectroscopy*, Oxford Book Company, Jaipur, India, 2009.

31 Y.-J. Song, M. Wang, X.-Y. Zhang, J.-Y. Wu and T. Zhang, *Nanoscale Res. Lett.*, 2014, **9**, 17.

32 F. M. Pontes, M. A. M. A. Maurera, A. G. Souza, E. Longo, E. R. Leite, R. Magnani, M. A. C. Machado, P. S. Pizani and J. A. Varela, *J. Eur. Ceram. Soc.*, 2003, **23**, 3001–3007.

33 A. Phuruangrat, T. Thongtem and S. Thongtem, *Superlattices Microstruct.*, 2012, **52**, 78–83.

34 C. Duan, Z. Zhang, S. Rösler, S. Rösler, A. Delsing, J. Zhao and H. T. Hintzen, *Chem. Mater.*, 2011, **23**, 1851–1861.

35 H. Yin, Y. Li, J. Bai, M. Ma and J. Liu, *J. Materiomics*, 2017, **3**, 144–149.

36 Z. Xia and W. Wu, *Dalton Trans.*, 2013, **42**, 12989–12997.

37 W. Deng, F. Chun, W. Li, H. Su, B. Zhang, M. Xie, H. Zhang, X. Chu, L. Jin, C. Luo and W. Yang, *Langmuir*, 2018, **34**, 8499–8507.

38 B. Xiao and M. Schmidt, *Inorg. Chem.*, 2017, **56**, 14948–14959.

39 P. Jena, S. K. Gupta, N. K. Verma, A. K. Singh and R. M. Kadam, *New J. Chem.*, 2017, **41**, 8947–8958.

40 X. Liu and J. Lin, *J. Mater. Chem.*, 2007, **18**, 221–228.

41 Z. Lou and M. Cocivera, *Mater. Res. Bull.*, 2002, **37**, 1573–1582.

42 G. Li, Z. Hou, C. Peng, W. Wang, Z. Cheng, C. Li, H. Lian and J. Lin, *Adv. Funct. Mater.*, 2010, **20**, 3446–3456.

43 Z. Gao, Y. Hu, W. Sun and J. W. Drelich, *Langmuir*, 2016, **32**, 6282–6288.

44 N. Kupka and M. Rudolph, *Int. J. Min. Sci. Technol.*, 2018, **28**, 373–384

45 W. Che, G. Li, X. Liu, K. Shao, D. Zhu, Z. Su and M. R. Bryce, *Chem. Commun.*, 2018, **54**, 1730–1733.

46 A. Singh, D. P. Dutta, J. Ramkumar, K. Bhattacharya, A. K. Tyagi and M. H. Fulekar, *RSC Adv.*, 2013, **3**, 22580–22590.

47 J. Liu, Y. Zhong, P. Lu, Y. Hong, J. W. Y. Lam, M. Faisal, Y. Yu, K. S. Wong and B. Z. Tang, *Polym. Chem.*, 2010, **1**, 426.

48 M. Kaur, S. K. Mehta and S. K. Kansal, *Spectrochim. Acta. A. Mol. Biomol. Spectrosc.*, 2017, **180**, 37–43.

49 N. Tripathi, S. Sandhu, P. Singh, A. Mahajan, M. Kaur and S. Kumar, *Sens. Actuators B Chem.*, 2016, **231**, 79–87.

50 K.-M. Wang, L. Du, Y.-L. Ma and Q.-H. Zhao, *Inorg. Chem. Commun.*, 2016, **68**, 45–49.

51 W. Na, X. Liu, S. Pang and X. Su, *RSC Adv.*, 2015, **5**, 51428–51434.

52 S. S. Nagarkar, A. V. Desai and S. K. Ghosh, *Chem. Commun.*, 2014, **50**, 8915–8918.

53 N. Dey, S. K. Samanta and S. Bhattacharya, *ACS Appl. Mater. Interfaces*, 2013, **5**, 8394–8400.

54 R.-X. Yao, X. Cui, X.-X. Jia, F.-Q. Zhang and X.-M. Zhang, *Inorg. Chem.*, 2016, **55**, 9270–9275.

55 A. B. Siddique, A. K. Pramanick, S. Chatterjee and M. Ray, *Sci. Rep.*, 2018, **8**, 1–10.

56 B. B. Campos, R. Contreras-Cáceres, T. J. Bandosz, J. Jiménez-Jiménez, E. Rodríguez-Castellón, J. C. G. Esteves da Silva and M. Algarra, *Carbon*, 2016, **106**, 171–178.

57 A. Sharma, D. Kim, J.-H. Park, S. Rakshit, J. Seong, G. H. Jeong, O.-H. Kwon and M. S. Lah, *Commun Chem*, 2019, **2**, 1–8.

58 J. Wang, J. Wu, L. Lu, H. Xu, M. Trivedi, A. Kumar, J. Liu and M. Zheng, *Front. Chem.*, 2019, **7**, 244.

59 C. Ambard, N. Duée, F. Pereira, D. Portehault, C. Méthivier, C.-M. Pradier and C. Sanchez, *J. Sol-Gel Sci. Technol.*, 2016, **79**, 381–388.

60 (a) H. Chen, A. Fang, L. He, Y. Zhang and S. Yao, *Talanta*, 2017, **164**, 580–587; (b) Y. Ling, N. Zhang, F. Qu, T. Wen, Z. F. Gao, N. B. Li and H. Q. Luo, *Spectrochim. Acta. A. Mol. Biomol. Spectrosc.*, 2014, **118**, 315–320.

61 (a) G. George, M. D. Simpson, B. R. Gautam, D. Fang, J. Peng, J. Wen, J. E. Davis, D. Ila and Z. Luo, *RSC Adv.*, 2018, **8**, 39296–39306; (b) G. George, S. L. Jackson, Z. R. Mobley, B. R. Gautam, D. Fang, J. Peng, D. Luo, J. Wen, J. E. Davis, D. Ila and Z. Luo, *J. Mater. Chem. C*, 2018, **6**, 7285–7294.

Graphical Abstract